First-Order Induced Current Density Imaging and Electrical Properties Tomography in MRI

Fuchs, Patrick S.; Mandija, Stefano; Stijnman, Peter R.S.; Brink, Wyger M.; van den Berg, Cornelis A.T.; Remis, Rob F.

DOI
10.1109/TCI.2018.2873407

Publication date
2018

Document Version
Accepted author manuscript

Published in
IEEE Transactions on Computational Imaging

First-Order Induced Current Density Imaging and Electrical Properties Tomography in MRI

Patrick S. Fuchs, Stefano Mandija, Peter R.S. Stijnman, Wyger M. Brink, Cornelis A.T. van den Berg, Rob F. Remis

***Abstract*—In this paper, we present an efficient dedicated electrical properties tomography algorithm (called *first-order current density EPT*) that exploits the particular radio frequency field structure, which is present in the midplane of a birdcage coil, to reconstruct conductivity and permittivity maps in this plane from $\hat{B}_1^+$ data. The algorithm consists of a current density and an electrical properties step. In the current density reconstruction step, the induced currents in the midplane are determined by acting with a specific first-order differentiation operator on the $\hat{B}_1^+$ data. In the electrical properties step, we first determine the electric field strength by solving a particular integral equation, and subsequently determine conductivity and permittivity maps from the constitutive relations. The performance of the algorithm is illustrated by presenting reconstructions of a human brain model based on simulated (noise corrupted) data and of a known phantom model based on experimental data. The method manages to reconstruct conductivity profiles without model related boundary artefacts and is also more robust to noise because only first-order differencing of the data is required as opposed to second-order data differencing in Helmholtz-based approaches. Moreover, reconstructions can be performed in less than a second, allowing for essentially real-time electrical properties mapping.**

***Index Terms*—Magnetic resonance imaging, electrical properties tomography, dielectric tissue properties, $\hat{B}_1^+$ field**

I. Introduction

The main objective of Electrical Properties Tomography (EPT) is to retrieve the conductivity and permittivity of tissue from B_1^+ data as measured by an MRI scanner. Knowledge about these parameters is extremely important in a wide variety of clinical applications. The conductivity is of potential importance as an endogenous biomarker in oncology [1] and acute stroke imaging [2], [3], for example, and the conductivity along with the electric field strength is also required to determine the Specific Absorption Rate (SAR) inside the human body [4] – [6].

Many different EPT methods have been developed over the years ranging from local differential equation approaches (see [7] – [12], for example) to methods that use global integral Green's tensor field representations in an optimization setting to find the dielectric tissue maps at the Larmor frequency of operation [13], [14]. The local differential-based EPT methods are direct noniterative reconstruction methods, often based on the Helmholtz equation for the radio frequency (RF) magnetic field. Standard Helmholtz-based EPT (MR-EPT) [8]requires a constant dielectric profile and second-order spatial differentiation of the data. Care must be taken when implementing this differentiation operation to mitigate noise amplification [3], [15], [16]. On the other hand, in the global integral-based approach the dielectric tissue parameters are determined in an iterative manner by minimizing an objective function. Here, integral operators act on the data, which makes the method more robust to noise. A disadvantage of the global approach is that it is more complex to implement than a direct method and its computational costs are generally much higher. However, strongly inhomogeneous tissue profiles are easily incorporated in a global method and regularization can be added to the objective function to further suppress the effects of noise.

A number of EPT methods have been developed for two-dimensional datasets [13], [16], [19], whereas there are also methods that work on fully three-dimensional $\hat{B}_1^+$ data sets [14], [20]. We shall focus on two-dimensional measurements, as it has

Submitted 5th Feb, 2018 to IEEE Transactions on Computational Imaging

P.S. Fuchs and R.F. Remis are with the Circuits and Systems group at the Delft University of Technology, Mekelweg 4, 2628CD Delft, The Netherlands. Stefano Mandija, P.R.S. Stijnman and C.A.T. van den Berg are with Centre of Image Sciences at the University Medical Center Utrecht, Utrecht, The Netherlands. W.M. Brink is with the C.J. Gorter Center for High Field MRI at the Leiden University Medical Center, Leiden, The Netherlands. (correspondence e-mail: P.S.Fuchs@tudelft.nl)

been shown [21] that the RF field is essentially E-polarized in the midplane of a birdcage coil, meaning that the electric field strength is mainly directed in the longitudinal z-direction, while the magnetic field strength has transverse x- and y-components only. In this paper, we present a dedicated EPT method that exploits this particular field structure.

In particular, in our first-order induced current EPT method (foIC-EPT) we exploit the structure of the RF field and obtain the induced current density by acting with a particular first-order differential operator on collected $\hat{B}_1^+$ data. Since this operation provides us with an image of the currents that are induced in tissue that is present in the (mid)plane of interest, we call this step the *induced current reconstruction step* of our method. We note that current density imaging in the context of the Helmholtz equation has also been investigated in [22], for example.

In the second *electrical properties step* of our method, the conductivity and permittivity maps are reconstructed by first computing the electric field strength and subsequently employing the constitutive relations between the induced currents and the electric field strength. Our foIC-EPT can therefore be seen as a hybrid method, in which a local differentiation operator is used to obtain the currents and a global integral operator is used to obtain the electric field.

Similar to most of the EPT approaches mentioned above, the foIC-EPT method relies on the transceive phase approximation [17] to obtain conductivity and permittivity reconstructions from $\hat{B}_1^+$ data. The effects of this approximation on the reconstructions is presently not fully understood and application of this approximation may result in reconstruction errors. A possible reconstruction strategy for iterative volume-integral EPT methods that overcomes this drawback has been reported in [18], however.

Finally, we note that foIC-EPT is a dedicated EPT method, in the sense that it exploits the particular field structure that is present in the midplane of a birdcage coil. This makes the method very efficient and it produces images of the induced current density and conductivity and permittivity maps with no boundary artefacts related to any underlying assumptions on the electrical property distribution and essentially in real time even on a standard PC or laptop (e.g. on an Intel i5 PC with 8Gb of RAM).

II. Induced Current Density Imaging

In this section, we describe the induced current step of our EPT algorithm. This step is based on the observation presented in [21] that the RF field in the midplane of a birdcage coil is essentially E-polarized. We therefore follow [13], [19], and [21] and consider E-polarized RF fields governed by the Maxwell equations

$$-\partial_x \hat{B}_y + \partial_y \hat{B}_x + \mu_0 \hat{J}_z^{\text{ind}} = 0, \tag{1}$$

$$\partial_y \hat{E}_z + \mathrm{j}\omega \hat{B}_x = 0, \tag{2}$$

and

$$-\partial_x \hat{E}_z + \mathrm{j}\omega \hat{B}_y = 0, \tag{3}$$

where $\hat{J}_z^{\text{ind}} = (\sigma + \mathrm{j}\omega\varepsilon)\hat{E}_z$ is the induced current density. This density can be imaged in a straightforward manner from available $\hat{B}_1^+$ data where $\hat{B}_1^+$ is given by

$$\hat{B}_1^+ = \frac{\hat{B}_x + \mathrm{j}\hat{B}_y}{2}. \tag{4}$$

Specifically, introducing the operator

$$\partial^- = \partial_x - \mathrm{j}\partial_y, \tag{5}$$

we have

$$\partial^- \hat{B}_1^+ = \frac{1}{2}\left[\partial_x \hat{B}_x + \partial_y \hat{B}_y - \mathrm{j}\left(\partial_y \hat{B}_x - \partial_x \hat{B}_y\right)\right] \tag{6}$$

and using equation (1) and $\partial_x \hat{B}_x + \partial_y \hat{B}_y = 0$, we arrive at

$$\hat{J}_z^{\text{ind}} = \frac{2}{\mathrm{j}\mu_0}\partial^- \hat{B}_1^+. \tag{7}$$

This is our basic imaging formula. Since it is based on the first-order Maxwell system, only first-order differentiation operators act on $\hat{B}_1^+$ data and since there are no additional (higher-order) differentiation operations in the following second step of our method (see Section III), the entire method only contains first-order differentiation operators, as opposed to EPT techniques which are based on second-order (Helmholtz) equations, where a second-order differentiation operator (Laplacian) is applied to the data. The above imaging formula is therefore less sensitive to perturbations or noise and, since the differentiation kernel is smaller, boundary artefacts related to the discrete nature of the finite differencing kernel are also less severe compared

with second-order approaches. Lastly, no assumptions on the electrical properties have been made in the definition of the induced currents, whereas Helmholtz based methods have to assume constant dielectric parameters.

III. Electrical Properties Reconstruction

Up to this point, we have addressed imaging of the induced current density inside the human body. This density depends on the external sources through the fields that are excited by these sources. The conductivity and permittivity parameters are intrinsic properties of tissue that do not depend on the external sources. To retrieve the tissue parameters, we therefore have to take the presence of the external sources into account. To this end, we set up a volume-integral scattering formalism (see, for example, [23] – [25]) and define the incident RF field $\{\hat{B}_x^{\text{inc}}, \hat{B}_y^{\text{inc}}, \hat{E}_z^{\text{inc}}\}$ as the field that is present in an empty (air-filled) birdcage coil. The scattered magnetic field $\{\hat{B}_x^{\text{sc}}, \hat{B}_y^{\text{sc}}, \hat{E}_z^{\text{sc}}\}$ is introduced as the difference between the total field and the incident field. Specifically,

$$\{\hat{B}_x^{\text{sc}}, \hat{B}_y^{\text{sc}}, \hat{E}_z^{\text{sc}}\} = \{\hat{B}_x, \hat{B}_y, \hat{E}_z\} - \{\hat{B}_x^{\text{inc}}, \hat{B}_y^{\text{inc}}, \hat{E}_z^{\text{inc}}\} \quad (8)$$

and the scattered electric field due to the presence of the body is given by (see [23] – [25], for example)

$$\hat{E}_z^{\text{sc}}(\boldsymbol{\rho}) = \mathrm{j}\omega\mu_0 \int_{\boldsymbol{\rho}'\in\mathbb{D}} \hat{G}(\boldsymbol{\rho}-\boldsymbol{\rho}')\, \hat{J}_z^{\text{sc}}(\boldsymbol{\rho}')\, \mathrm{d}V. \quad (9)$$

This integral representation holds for all observation points in the midplane of the body coil. Furthermore,

$$\hat{G}(\boldsymbol{\rho}) = -\frac{\mathrm{j}}{4} H_0^{(2)}(k_0|\boldsymbol{\rho}|) \quad (10)$$

is the Green's function of the homogeneous background medium (air) with $k_0 = \omega/c_0$ its corresponding wave number and $H_0^{(2)}$ the Hankel function of the second kind and order zero. Finally, $\hat{J}_z^{\text{sc}}$ is the scattering source given by

$$\hat{J}_z^{\text{sc}} = \begin{cases} \hat{J}_z^{\text{ind}} - \mathrm{j}\omega\varepsilon_0\hat{E}_z & \text{for } \boldsymbol{\rho}\in\mathbb{D}, \\ 0 & \text{for } \boldsymbol{\rho}\notin\mathbb{D}, \end{cases} \quad (11)$$

where $\mathbb{D}$ is the body domain. Substituting this scattering source (Eq. (11)) in the integral representation of Eq. (9), using the imaging equation (7), and the definition of the scattered electric field strength ($\hat{E}_z^{\text{sc}} = \hat{E}_z - \hat{E}_z^{\text{inc}}$), we find that the electric field satisfies

$$\hat{E}_z(\boldsymbol{\rho}) + k_0^2 \int_{\boldsymbol{\rho}'\in\mathbb{D}} \hat{G}(\boldsymbol{\rho}-\boldsymbol{\rho}')\, \hat{E}_z(\boldsymbol{\rho}')\, \mathrm{d}V = \hat{f}(\boldsymbol{\rho}), \quad (12)$$

where the right-hand side is given by

$$\hat{f}(\boldsymbol{\rho}) = \hat{E}_z^{\text{inc}}(\boldsymbol{\rho}) - 2\omega \int_{\boldsymbol{\rho}'\in\mathbb{D}} \hat{G}(\boldsymbol{\rho}-\boldsymbol{\rho}')\, \partial^- \hat{B}_1^+(\boldsymbol{\rho}')\, \mathrm{d}V \quad (13)$$

and $\boldsymbol{\rho}\in\mathbb{D}$. Observe that the right-hand side $\hat{f}$ of Eq. (12) is known and with $\boldsymbol{\rho}\in\mathbb{D}$, Eq. (12) is an integral equation for the electric field strength in $\mathbb{D}$ which can be solved iteratively using the generalized minimal residual (GMRES) solver, for example [26]. Also note that local noise effects in $\partial^-\hat{B}_1^+$ are smoothed or smeared out through integration over the body domain. Smoothing is predominantly local, however, because of the singularity of the Green's function at $\boldsymbol{\rho}' = \boldsymbol{\rho}$.

After solving integral equation (12), we have the electric field strength at our disposal and the conductivity and permittivity maps at frequency ω can be determined by using the constitutive relation

$$\hat{J}_z^{\text{ind}}(\boldsymbol{\rho}) = [\sigma(\boldsymbol{\rho}) + \mathrm{j}\omega\varepsilon(\boldsymbol{\rho})]\, \hat{E}_z(\boldsymbol{\rho}), \quad (14)$$

for $\boldsymbol{\rho}\in\mathbb{D}$, since both $\hat{J}_z^{\text{ind}}(\boldsymbol{\rho})$ and $\hat{E}_z(\boldsymbol{\rho})$ are now known. Explicitly, by equating the real and imaginary parts of the above equation, we obtain the conductivity profile

$$\sigma(\boldsymbol{\rho}) = \frac{2}{\mu_0|\hat{E}_z(\boldsymbol{\rho})|^2}\ \mathrm{Im}\left[\hat{E}_z^*(\boldsymbol{\rho})\, \partial^-\hat{B}_1^+(\boldsymbol{\rho})\right], \quad (15)$$

while the permittivity profile is given by

$$\varepsilon(\boldsymbol{\rho}) = \frac{-2}{\omega\mu_0|\hat{E}_z(\boldsymbol{\rho})|^2}\ \mathrm{Re}\left[\hat{E}_z^*(\boldsymbol{\rho})\, \partial^-\hat{B}_1^+(\boldsymbol{\rho})\right], \quad (16)$$

where the asterisk denotes complex conjugation. Note that the conductivity and permittivity can only be retrieved at points $\boldsymbol{\rho}\in\mathbb{D}$ where the electric field strength does not vanish.

Our overall electrical properties tomography approach can now be summarized as follows:

First-Order Induced Current Density EPT Algorithm (foIC-EPT)

* **Input:**

- $\hat{B}_1^+$ field data

- The z-component of the incident electric field strength $\hat{E}_z^{\text{inc}}$

1) **Induced current step:** Determine the induced electric current density using equation (7).

2) **Electrical properties step:**
   - Solve integral equation (12) for the electric field strength.
   - Determine the conductivity and permittivity maps using equations (15) and (16).

Note that the z-component of the incident electric field strength is not required to carry out induced current step 1, but is required to carry out electrical properties step 2.

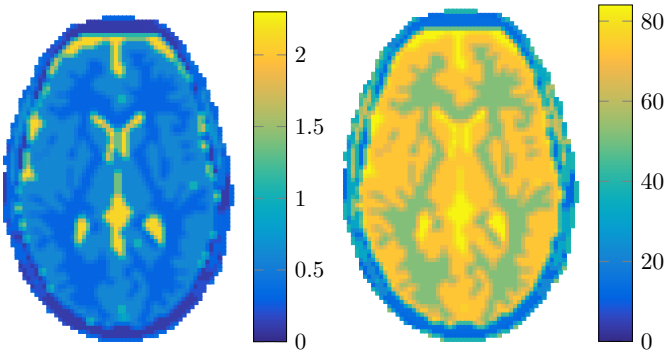

Fig. 1: Conductivity map in S/m (left) and relative permittivity map (right) of the center slice head model.

IV. Simulation and Experiment

In this section, we illustrate the performance of foIC-EPT using simulated and measured $\hat{B}_1^+$ data. Specifically, we apply foIC-EPT to simulated $\hat{B}_1^+$ data collected inside the head of the female body model Ella of the IT'IS foundation [27] and corrupt this data with noise. Subsequently, we apply the foIC-EPT algorithm to measured $\hat{B}_1^+$ data obtained for a cylindrical inhomogeneous phantom.

A. Imaging based on simulated data

The head model of the IT'IS foundation has a voxel size of 2.5 mm^3 isotropic and the conductivity and permittivity maps of the slice that coincides with the midplane of the birdcage coil are shown in Fig. 1. The coil and corresponding incident field are simulated by positioning 16 line sources uniformly on a circle that is concentric to the head model. The radius of this circle is 34 cm and the line sources operate in quadrature mode at a frequency of 128 MHz, which corresponds to the operating frequency of a 3T MRI scanner. The simulation was performed at the same resolution as the phantom (2.5 mm^3 isotropic), and the simulation was programmed in MATLAB 2015b (The MathWorks, Inc., Natick, Massachusetts, United States) using an in-house simulation code. Furthermore, we corrupt the $\hat{B}_1^+$ data by complex white Gaussian noise such that we have a Signal-to-Noise Ratio (SNR) of 20 dB (100 on a linear scale).

Since the conductivity and permittivity maps of the body model are known in this example, we can numerically compute the exact induced current density within our slice of interest. The magnitude of this current density is shown in Fig. 2 (left), while the reconstruction based on imaging formula (7) is shown in Fig. 2 (middle). The pointwise relative error between the numerically computed induced current density and the reconstructed density is shown in Fig. 2 (right). We observe that the largest errors occur near the interfaces between different tissue types, especially at the outer regions of the head. Furthermore, there is a large error in the center of the reconstruction, which is due to a low E-field at this location, that exacerbates the presence of noise in the data. Sensitivity to noise is not as severe as in Helmholtz-based approaches, however, since in the latter approaches a second-order differentiation operator (Laplacian) acts on the data, while in our induced current step only the first-order derivative of collected $\hat{B}_1^+$ data is computed. For differencing a first order forward kernel was used, which would lead to single voxel boundary artefacts if the measured data would be perfectly masked to the size of the head. However, in this simulation this mask was chosen one voxel larger to remove this purely numerical error.

To suppress the effects of noise that is present in the input data, we now first filter this data using a five-point (5×5) Gaussian image filter with mean zero and variance 2. This will lead to some loss of spatial resolution, but will reduce the noise amplification effect due to differentiation of the data. A median filter has also been applied and works well in preserving edge information in high SNR regions, but creates artefacts in low SNR regions due to the nonlinear nature of the filter and the smooth nature of the B_1^+ map.

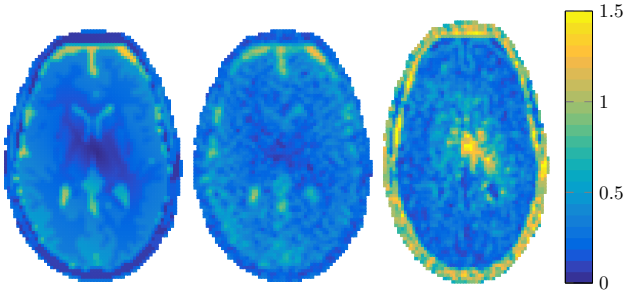

Fig. 2: Magnitude of the exact induced current density $\hat{J}_z^{\text{ind}}$ in the center slice of the Ella head model (left), magnitude of the reconstructed current density using imaging formula (7) on noisy $\hat{B}_1^+$ data (middle), and the pointwise relative error of the reconstructed induced current density (right). The left and middle density plots have been normalized with respect to max $|\hat{J}_z^{\text{ind}}|$. The colorbar refers to the error plot.

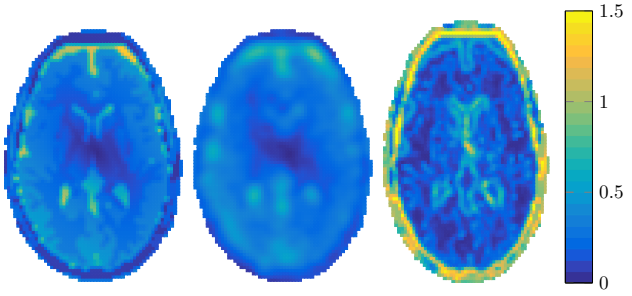

Fig. 3: Magnitude of the exact induced current density $\hat{J}_z^{\text{ind}}$ in the center slice of the Ella head model (left), magnitude of the reconstructed current density using imaging formula (7) on filtered noisy $\hat{B}_1^+$ data (middle), and the pointwise relative error of the reconstructed induced current density (right). The left and middle density plots have been normalized with respect to max $|\hat{J}_z^{\text{ind}}|$. The colorbar refers to the error plot.

Subsequently, we apply equation (7) on the filtered data to obtain the reconstructed induced current density as shown in Fig. 3 (middle) along with the exact current density and pointwise relative error shown in Fig. 3 (left) and Fig. 3 (right), respectively. The quality of our one-step imaging result has clearly improved and we therefore use the filtered $\hat{B}_1^+$ data to carry out the electrical properties step of foIC-EPT (step 2 of the foIC-EPT algorithm). Specifically, we use the filtered $\hat{B}_1^+$ data to compute the right-hand side $\hat{f}$ of equation (12) as given by equation (13). Having this right-hand side available,

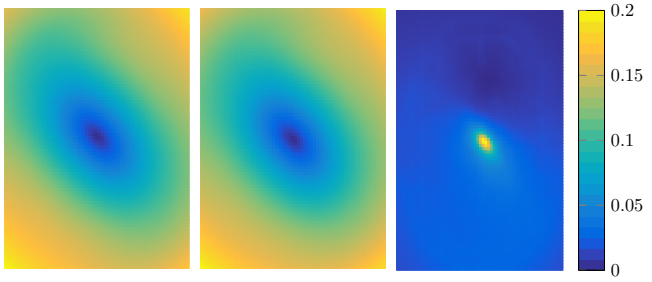

Fig. 4: Magnitude of the exact electric field strength $\hat{E}_z$ in the center slice of the Ella head model (left), magnitude of the reconstructed electric field strength based on filtered $\hat{B}_1^+$ data (middle), and the pointwise relative error of the reconstructed electric field strength (right). The left and middle field strength plots have been normalized with respect to max $|\hat{E}_z|$. The colorbar refers to the error plot.

we solve the integral equation of equation (12) using the GMRES algorithm. It takes about ten iterations to arrive at a normalized residual of 10^{-6} (matrix size 256×256) and the resulting electric field strength is shown in Fig. 4 (middle). The corresponding exact electric field strength is shown in Fig. 4 (left) and the pointwise relative error between the exact and reconstructed electric fields is shown in Fig. 4 (right). Overall, the electric field strength is fairly well reconstructed, except at the center of the slice, where the magnitude of the exact electric field strength essentially vanishes. For antennas in a birdcage setting and operating in quadrature mode, it is well known that the magnitude of the electric field strength is small in a neighborhood of the center of the slice (see [13], for example) and it is difficult to accurately reconstruct this field based on noisy $\hat{B}_1^+$ input data [28].

Having reconstructed the electric field strength from $\hat{B}_1^+$ data, we can determine the conductivity and permittivity maps using equations (15) and (16), respectively. The reconstructed conductivity map is shown in Fig. 5 (right), while the reconstructed permittivity map is shown in Fig. 6 (right). Reconstructions of the conductivity and permittivity maps based on noiseless $\hat{B}_1^+$ data are shown in Fig. 5 (middle) and Fig. 6 (middle), respectively, thereby highlighting the effects of noise on the conductivity and permittivity reconstructions. In particular, for noisy data smooth reconstructions are obtained due to filtering and for both noiseless and noisy data the error is maximum around the center of the slice,

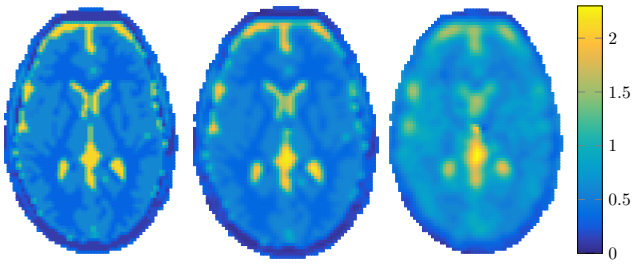

Fig. 5: Original (left) and reconstructed conductivity maps in S/m based on noiseless (middle) and noisy (right) $\hat{B}_1^+$ data.

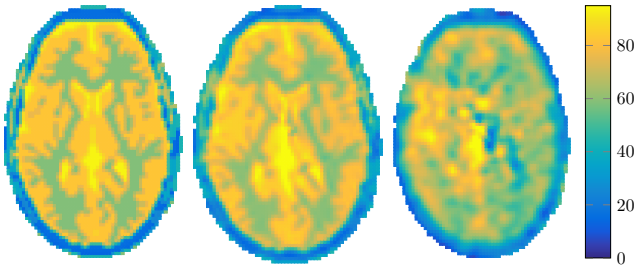

Fig. 6: Original (left) and reconstructed relative permittivity maps based on noiseless (middle) and noisy (right) $\hat{B}_1^+$ data.

since the error in the reconstruction of the electric field strength is maximum in this neighborhood and the magnitude of the electric field strength is small at this location as well. A low E-field leads to induced electric currents $\hat{J}_z^{\text{ind}}$ that give a small to negligible contribution to the $\hat{B}_1^+$ field and reconstructing the conductivity and permittivity at such locations is therefore very challenging. Finally, we mention that it takes our implementation of the overall foIC-EPT algorithm less than a second to retrieve the conductivity and permittivity maps from the collected $\hat{B}_1^+$ data on an Intel i5 PC with 8Gb of RAM.

B. Imaging based on measured data

In this experiment, we use a 1.5% agar based cylindrical phantom filled with saline water to validate our foIC-EPT method. The phantom consists of an inner and an outer cylinder with conductivities given by 0.95 S/m and 0.45 S/m, respectively, and a photograph of the phantom is shown in Fig. 7 (top). The conductivities were independently obtained using the Stogryn equation [29]. A 3T MRI System (Ingenia, Philips) and a 16 channel head coil (Philips Medical Systems, Best, The Netherlands) were used

TABLE I: Sequence parameters used for the phantom experiment

Parameters	SE sequence	AFI sequence	Unit
FoV	$200 \times 200 \times 2.5$	$200 \times 200 \times 9$	[mm^3]
Resolution	$2.5 \times 2.5 \times 2.5$	$2.5 \times 2.5 \times 3$	[mm^3]
Rep. time (TR)	1000	TR1: 50 TR2: 250	[ms]
Echo Time (TE)	5	2.7	[ms]
Water-fat shift / Bandwidth	$\frac{0.3}{1400}$	$\frac{0.9}{480}$	$[\frac{\text{pixels}}{\text{Hz}}]$
Flip angle	90	65	[°]
Signal averages	10	10	[#]

to obtain the $\hat{B}_1^+$ data shown in Fig. 7 (bottom). The amplitude of the $\hat{B}_1^+$ field was measured using the Actual Flip-angle Imaging (AFI) method [30], while the transceive phase was measured using two single Spin Echo (SE) sequences with opposing readout polarities [3], [7], [17], [31]. Both sequences were carried out with 10 signal averages, and the field of view is centered at the middle of the coil. Parameter settings of the measurement sequences can be found in Table 1. Furthermore, the phantom was placed at the center, and the system's body coil was used for transmitting, while a head coil was used for reception. To remove the impact of the complex sensitivity of the head coil, the receive array data was phase-referenced to the body coil using a built-in routine. In this way, the transmit and receive phase of the birdcage coil determines the observed transceive phase [3], [7], [17], [31]. Subsequently, the transceive phase approximation was applied [3], [7], [17], [31] to obtain an approximate $\hat{B}_1^+$ phase from the measured transceive phase. Finally, the SNR of the measured data is 17.75 dB (approx. 60 on a linear scale) and 18.75 dB (approx. 75 on a linear scale) for the amplitude and phase scans, respectively.

Having the complex $\hat{B}_1^+$ data map available, we use the foIC-EPT algorithm to reconstruct the conductivity and permittivity maps of the phantom by essentially following the same steps as in the previous subsection. In particular, first the data is filtered using a Gaussian filter and subsequently the induced current density $\hat{J}_z^{\text{ind}}$ is determined using the imaging formula of equation (7). The magnitude of the reconstructed current within the reconstruction area is shown in Fig. 8 (left). In addition, we simulated the $\hat{B}_1^+$ field using the Sim4Life software package (ZMT, Zurich, Switzerland) and reconstructed the in silico induced currents using equation (7). The

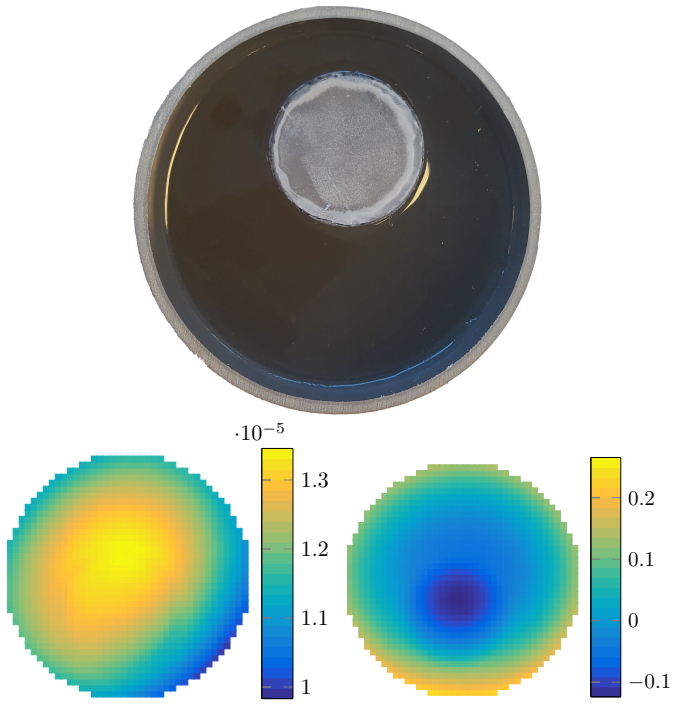

Fig. 7: Photograph of the phantom (top), the masked amplitude of the measured $\hat{B}_1^+$ field (bottom left), and the masked measured transceive phase (bottom right).

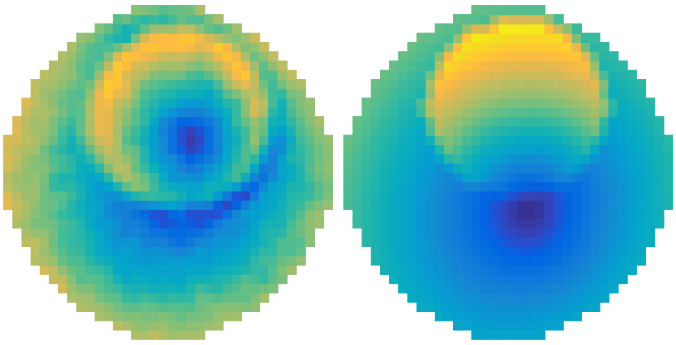

Fig. 8: Magnitude of the induced current based on measured data (left) and magnitude of the in silico induced-current based on simulated data (right).

magnitude of the in silico induced current is shown in Fig. 8 (right). Clearly, there is a mismatch at the center of the inner compartment and at its boundary. This mismatch will be discussed further below in combination with the conductivity reconstruction and is also investigated in [18].

To carry out the second step of our reconstruction method, the incident electric field in the imaging plane of interest is required to determine the right-hand side of equation (12). This field was computed using the Sim4Life software package (ZMT, Zurich, Switzerland) obviously using the same configuration as for the in-silico induced current simulations. Having determined the field vector $\hat{f}$, we solve the integral equation for the total electric field using the GMRES iterative solver. For this particular configuration, it takes the solver a fraction of a second on an Intel i5 PC with 8 Gb of RAM to solve the integral equation in six iterations reaching a normalized residual of 10^{-6}. With the electric field strength now at our disposal, we can determine the conductivity and permittivity profiles of the phantom using equations (15) and (16) . The reconstructions are shown in the top row of Fig. 9 along with Helmholtz reconstructions shown in the bottom row of Fig. 9. The Helmholtz reconstructions were obtained using a smoothed phase-only implementation from [16], [17] that employs a 7×3 finite differencing kernel.

We observe that foIC-EPT provides a good overall reconstruction and jumps in the conductivity profile are well resolved. Only small local dips are present in the conductivity profile near the center of the inner cylinder and to the lower right of the center of the imaging area. These local dips correspond to locations where the reconstructed induced current density is small as well (see Fig. 8 (left)). Preliminary studies indicate that these dips are due to the application of the transceive phase approximation, but further testing is necessary to confirm these findings. Nevertheless, a good overall agreement with the exact conductivity profile is obtained when using foIC-EPT even in case the transceive approximation is applied. The Helmholtz-based approach, on the other hand, suffers from ripple or edge effects as is evident from the ring-shaped anomaly around the inner cylinder. Such effects are typically observed in standard Helmholtz-based reconstruction approaches as discussed in [8], [16], and [17], for example. The foIC-EPT method does not suffer from such boundary artefacts and is able to reconstruct the piecewise-constant conductivity profile.

The permittivity reconstructions obtained with foIC-EPT and MR-EPT are shown in Figs. 9b and 9d, respectively. In both cases, the reconstructions are poor compared with the quality of the conductivity reconstructions. This should not come as a surprise, however, since permittivity reconstructions are generally very sensitive to perturbations and noise in the data especially at 3T. More reliable permittivity reconstructions are probably obtained at 7T

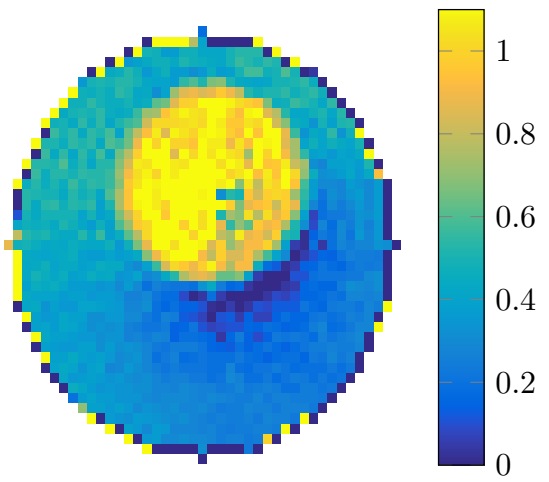

(a) foIC-EPT conductivity reconstruction in S/m.

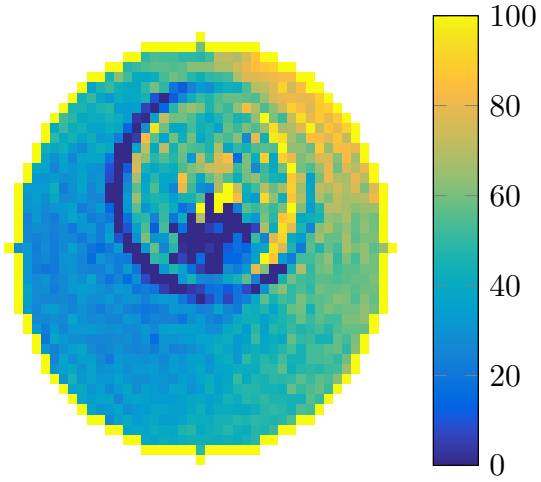

(b) foIC-EPT relative permittivity reconstruction.

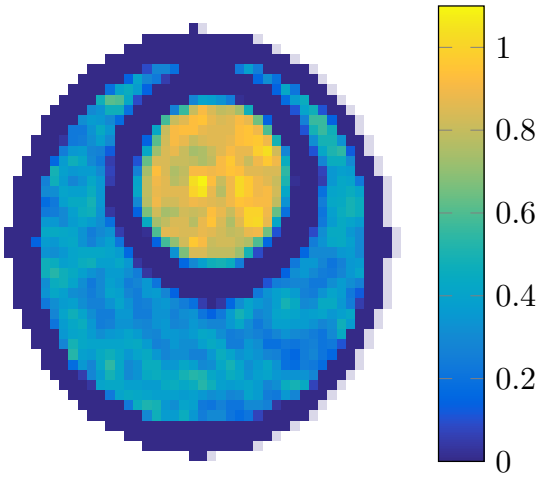

(c) MREPT conductivity reconstruction in S/m.

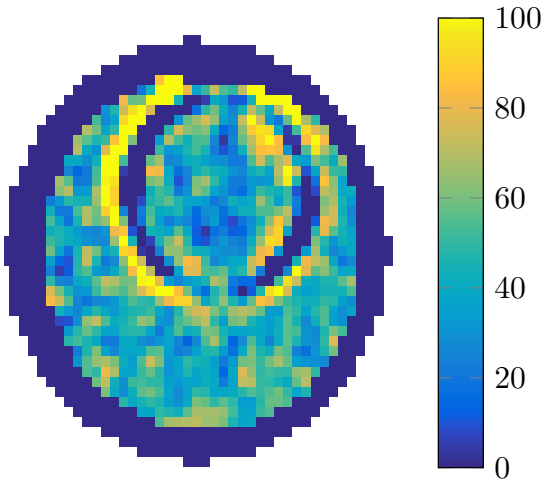

(d) MREPT relative permittivity reconstruction.

Fig. 9: Reconstructed conductivity maps in S/m and reconstructed relative permittivity maps. The true conductivity of the inner cylinder is 0.95 S/m, while the outer cylinder has a conductivity of 0.45 S/m. The true relative permittivity of the inner and outer cylinder is estimated to be around 80.

or even higher field strengths. Finally, we mention that for this phantom experiment the computation times of foIC-EPT and the Helmholtz approach are 0.041 seconds and 0.027 seconds, respectively, on a standard PC with an Intel i5 (3.1GHz) and 8Gb of RAM.

V. Discussion and Conclusions

In this paper, we have presented a two-step electrical properties tomography technique (foIC-EPT) to reconstruct the conductivity and permittivity maps of tissue based on $\hat{B}_1^+$ data collected within the midplane of a birdcage coil. The first step consists of reconstructing the induced currents in the midplane of the coil using measured $\hat{B}_1^+$ data. From the first-order Maxwell equations it follows that these currents can be obtained by acting with a particular first-order differential operator on the collected data. Since only first-order differentiation operators are involved, foIC-EPT is less sensitive to noise compared with (Helmholtz) approaches, where second-order differential operators act on the data.

Having obtained the induced currents from step 1, step 2 consists of computing the electric field inside the plane of interest by solving a particular integral equation. Iterative solvers are particularly well suited for this task, since the integral that appears in this equation is a spatial convolution

integral and FFTs can be used to compute matrix-vector products at "FFT-speed." Computationally, this is the most expensive part of the foIC-EPT method, but the examples presented in this paper and additional numerical testing indicates that when the GMRES iterative solver is used, typically less than ten iterations are required to reach an error level of 10^{-6}.

After solving the integral equation, the conductivity and permittivity maps can be determined using the induced current density from step 1 and the constitutive relations. For realistic reconstruction problems using simulated or measured data, the complete reconstruction procedure (step 1 and 2) requires a fraction of a second to complete on a standard PC with an Intel i5 processor running at 3.2 GHz and having 8 Gb of RAM. This is a significant speed up compared with other optimization-based volume integral equation approaches such as CSI-EPT [13] or the method presented in [14], which typically require tens of seconds or even minutes to arrive at two-dimensional reconstructed conductivity and permittivity maps. We conclude that exploiting field structure in foIC-EPT results in a significant speed up, but also makes the method more restrictive than general volume integral approaches, which do not rely on any particular field structure.

Furthermore, in contrast with the CSI-EPT formulation, we only formulate a volume integral equation for the electric field and take the induced currents as given by Eq. (7) into account. This is different from CSI-EPT, where the contrast and contrast source (product of the contrast and the electric field) are both unknown and iteratively updated. Here, we already know the induced currents by exploiting the E-polarized field structure.

As opposed to Helmholtz-based approaches, foIC-EPT, as well as other volume-integral reconstruction methods, can handle jumps in the conductivity and permittivity profiles. No assumptions on the homogeneity of the object have to be imposed and no ripple or edge effects as in Helmholtz-based approaches are observed. However, what foIC-EPT has in common with some other non-Helmholtz-based EPT reconstruction methods is that reconstructions may be poor in regions where the amplitude of the electric field is low. To remedy this situation, active or passive shimming techniques can be applied as discussed in [13] and [19], for example. What the present foIC-EPT method also has in common with many other EPT reconstruction methods is that it relies on the transceive phase approximation, which introduces errors in the reconstructions as well. Numerical simulations and actual experiments indicate that this approximation is responsible for local dips in the reconstructed tissue profiles, but further testing is required. Present and future work focuses on developing an iterative volume-integral EPT reconstruction method that does not rely on the transceive approximation. Preliminary results are promising and have been presented in [18]. Moreover, local dips and variations in reconstructed tissue profiles may also be reduced or even eliminated by incorporating additional regularization strategies such as Total Variation (see [13], for example) into an EPT reconstruction method. Future work will focus on the implementation of such regularization techniques as well.

REFERENCES

[1] K. K. Tha, U. Katscher, S. Yamaguchi, C. Stehning, S. Terasaka, N. Fujima, K. Kudo, K. Kazumata, T. Yamamoto, M. Van Cauteren, H. Shirato, "Noninvasive electrical conductivity measurement by MRI: a test of its validity and the electrical conductivity characteristics of glioma," *Eur. Radiol.*, vol. 28, no. 1, pp. 348 – 355, 2017.

[2] L. X. Liu, W. W. Dong, X. M. Ji, L. H. Chen, L. Chen, W. He, J. P. Jia, "A new method of non-invasive brain-edema monitoring in stroke: cerebral electrical impedance measurement," *Neurol Res*, vol. 28, no. 1, pp. 31 – 37, 2006.

[3] U. Katscher, C. A. T. van den Berg, "Electric properties tomography: biochemical, physical and technical background, evaluation and clinical applications, *NMR Biomed.*," vol. 30, no. 8, pp. 1–15, 2017.

[4] J. Chen, Z. Feng, J. M. Jin, "Numerical simulation of SAR and B1-field inhomogeneity of shielded RF coils loaded with the human head," *IEEE Trans. Biomed. Eng.*, vol. 45, no. 5, pp. 650 – 659, 1998.

[5] C. M. Collins, W. Liu, J. Wang, R. Gruetter, J. T. Vaughan, K. Ugurbil, M. B. Smith, "Temperature and SAR calculations for a human head within volume and surface coils at 64 and 300 MHz," *J. Magn. Reson. Imaging*, vol. 19 no. 5, pp. 650 – 656, 2004.

[6] E. Balidemaj, C. A. T. van den Berg, A. L. H. M. W. van Lier, A. J. Nederveen, L. .J. A. Stalpers, H. Crezee, R. F. Remis, "B1-based SAR reconstruction using contrast source inversion—electric properties tomography (CSI-EPT)," *Med. Biol. Eng. Comput.*, vol. 55, no. 2, pp. 225 – 233, 2017.

[7] U. Katscher, T. Voigt, C. Findeklee, P. Vernickel, K. Nehrke, O. Dössel, "Determination of electrical conductivity and local SAR via B1 mapping, *IEEE Trans. Med. Imag.*," vol. 28, no. 9, pp. 1365 – 1374, 2009.

[8] J. Liu, Y. Wang, U. Katscher, B. He, "Electrical Properties Tomography Based on B_1 Maps in MRI: Principles, Applications, and Challenges", *IEEE Trans. Biomed. Eng.*, vol 64, no. 11, pp. 2515-2530, 2017.

[9] S. Bulumulla, S. K. B. Lee, T. B. Yeo, "Conductivity and permittivity imaging at 3.0 T", *Conc. in Magn. Reson. Part B (Magn. Reson. Eng.)*, vol 41(B), no. 1, pp. 13 – 21, 2012.

[10] N. Gürler, Y. Z. Ider, "Gradient-based electrical conductivity imaging using MR phase", *Magn. Reson. Med.*, vol 77, pp. 137 – 150, 2017.

[11] J. K. Seo, M. O. Kim, J. Lee, N. Choi, E. J. Woo, H. J. Kim, O. I. Kwon, D. H. Kim, "Error analysis of nonconstant admittivity for MR-based electric property ımaging", *IEEE Trans. Med. Imag.*, vol. 31, pp. 430 – 7, 2012.

[12] J. Liu, X. Zhang, S. Schmitter, P. F. van de Moortele, B. He, "Gradient-based electrical properties tomography (gEPT): a robust method for mapping electrical properties of biological tissues in vivo using magnetic resonance imaging," *Magn. Reson. Med.*, vol. 74, no. 3, pp. 634 – 646, 2015.

[13] E. Balidemaj, C. A. T. van den Berg, J. Trinks, A. L. H. M. W. van Lier, A. J. Nederveen, L. .J. A. Stalpers, H. Crezee, R. F. Remis, "CSI-EPT: A contrast source inversion approach for improved MRI-based electrical properties tomography," *IEEE Trans. Med. Imag.*, vol. 34, no. 9, pp. 1788 – 1796, 2015.

[14] R. Hong, S. Li, J. Zhang, Y. Zhang, N. Liu, Z. Yu, and Q. H. Liu, "3-D MRI-based electrical properties tomography using the volume integral equation method," *IEEE Trans. Microw. Techn.*, vol. 65, no. 12, pp. 4802 – 4811, Dec. 2017.

[15] S. K. Lee, S. Bulumulla, I. Hancu, "Theoretical investigation of random noise-limited signal-to-noise ratio in MR-based electrical properties tomography", *IEEE Trans. Med. Imag.*, vol 34, no. 11, pp. 2220 – 2232, 2015.

[16] S. Mandija, A. Sbrizzi, U. Katscher, P. R. Luijten, C. A. T. van den Berg, "Error analysis of Helmholtz-based MR-electrical properties tomography," *Magn Reson Med.*, 2017.

[17] A. L. H. M. W. van Lier, D. O. Brunner, K. P. Pruessmann, D. W. J. Klomp, P. R. Luijten, J. W. Langendijk, C. A. T. van den Berg, "B_1^+ phase mapping at 7T and its application for in vivo electrical conductivity mapping," *Magn. Reson. Med.*, vol. 67. no. 2, pp. 552 – 561, 2012.

[18] P. R. S. Stijnman, S. Mandija, P. S. Fuchs, R. F. Remis, C. A. T. van den Berg, "Transceive Phase Corrected Contrast Source Inversion-Electrical Properties Tomography", *In: Proc. of the ISMRM Joint Annual Meeting, 16-21 June 2018, Paris*; Paris, ISMRM, no. 5087, 1 Jun 2018.

[19] R. Schmidt, A. G. Webb, "A new approach for electrical properties estimation using a global integral equation and high permittivity materials," *J. Magn. Reson.*, vol. 262, pp. 8 – 14, 2016.

[20] R. L. Leijsen, W. M. Brink, C. A. T. van den Berg, A. G. Webb, and R. F. Remis, "Three-dimensional contrast source inversion – electrical properties tomography," *IEEE Trans. Med. Imag.*, accepted, 2018.

[21] B. van den Bergen, C. C. Stolk, J. B. van den Berg, J. J. W. Lagendijk, C. A. T. van den Berg, "Ultra fast electromagnetic field computations for RF multi-transmit techniques in high field MRI," *Phys. Med. Biol.*, vol. 54, no. 5, pp. 1253 – 1264, 2009.

[22] G. C. Scott, M. L. Joy, R. L. Armstrong, R. M. Henkelman, "RF current density imaging in homogeneous media", *Magn. Reson. Med.*, vol. 28, pp. 186 – 201, 1992.

[23] A. T. De Hoop, *Handbook of Radiation and Scattering of Waves*, London, Academic Press, 1995.

[24] C. A. Balanis, *Advanced Engineering Electromagnetics*, Hoboken, John Wiley and Sons, 2012.

[25] W. C. Chew, *Waves and Fields in Inhomogeneous Media*, New York, IEEE Press, 1995.

[26] Y. Saad, *Iterative Methods for Sparse Linear Aystems*, Philadelphia, SIAM, 2003.

[27] A. Christ, W. Kainz, E. G. Hahn, K. Honegger, M. Zefferer, E. Neufeld, W. Rascher, R. Janka, W. Bautz, J. Chen, "The virtual family development of surface based anatomical models of two addults and two children for dosimetric simulations," *Phys. Med. Biol.*, vol. 55, no. 2, pp. 23 – 38, 2010.

[28] F. S. Hafalir, O. F. Oran, N. Gurler, Y. Z. Ider, "Convection-reaction equation based magnetic resonance electrical properties tomography (cr-MREPT)", *IEEE Trans. Med. Imag.*, vol. 33, no. 3, pp. 777 – 793, 2014.

[29] A. Stogryn, "Equations for Calculating Dielectric Constant of Saline Water," *IEEE T Microw. Theory*, vol. 19, no. 8, pp. 733 – 736, 1971.

[30] V. L. Yarnykh, "Actual flip-angle imaging in the pulsed steady state: A method for rapid three-dimensional mapping of the transmitted radiofrequency field," *Magn. Reson. in Med.*, vol. 57 no. 1, pp. 192 – 200, 2007.

[31] H. Wen, "Noninvasive quantitative mapping of conductivity and dielectric distributions using RF wave propagation effects in high-field MRI", *In: Proc. SPIE Phys.f Med. Imag., 5 Jun 2003, San Diego*; San Diego, SPIE, no. 5030, 5 Jun 2003.